analytical chemistry

Editors' Choice

pubs.acs.org/ac

Article

Enzymatic Reactions Observed with Zero- and Low-Field Nuclear Magnetic Resonance

James Eills,* Román Picazo-Frutos, Oksana Bondar, Eleonora Cavallari, Carla Carrera, Sylwia J. Barker, Marcel Utz, Alba Herrero-Gómez, Irene Marco-Rius, Michael C. D. Tayler, Silvio Aime, Francesca Reineri, Dmitry Budker, and John W. Blanchard

Cite This: *Anal. Chem.* 2023, 95, 17997−18005

Read Online

ACCESS | Metrics & More | Article Recommendations | Supporting Information

ABSTRACT: We demonstrate that enzyme-catalyzed reactions can be observed in zero- and low-field NMR experiments by combining recent advances in parahydrogen-based hyperpolarization methods with state-of-the-art magnetometry. Specifically, we investigated two model biological processes: the conversion of fumarate into malate, which is used in vivo as a marker of cell necrosis, and the conversion of pyruvate into lactate, which is the most widely studied metabolic process in hyperpolarization-enhanced imaging. In addition to this, we constructed a microfluidic zero-field NMR setup to perform experiments on microliter-scale samples of [1-^{13}C]fumarate in a lab-on-a-chip device. Zero- to ultralow-field (ZULF) NMR has two key advantages over high-field NMR: the signals can pass through conductive materials (e.g., metals), and line broadening from sample heterogeneity is negligible. To date, the use of ZULF NMR for process monitoring has been limited to studying hydrogenation reactions. In this work, we demonstrate this emerging analytical technique for more general reaction monitoring and compare zero- vs low-field detection.

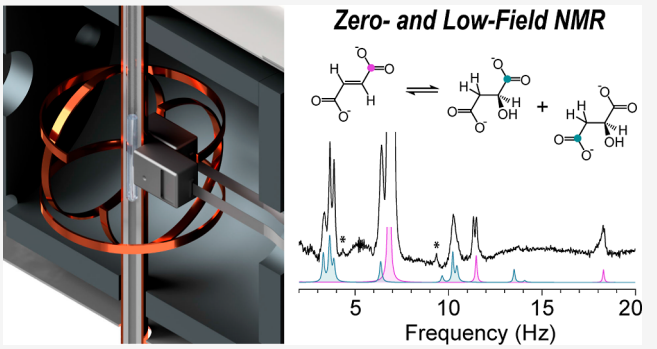

1. INTRODUCTION

Nuclear magnetic resonance (NMR) is among the most important spectroscopic techniques for chemical analysis and biochemical structure elucidation, and the imaging modality (MRI) is an invaluable diagnostic tool for noninvasive medical imaging. NMR has the potential to be even more widely applicable if the nuclear-spin polarization could be boosted beyond its thermal equilibrium value of $\sim 10^{-5}$ for samples at room temperature in experimentally achievable magnetic fields. In recent years, nuclear-spin hyperpolarization techniques—physical and chemical methods to increase NMR signals by 4−5 orders of magnitude[1−3]—have enabled a new application: hyperpolarized metabolic imaging.[4] Small molecules can be hyperpolarized and injected in vivo, and tracking their metabolism can yield diagnostic information about disease progression and treatment response.[5,6] Even with enhanced signals, conventional high-field magnetic resonance has some drawbacks: (1) high-resolution spectroscopy is generally only achievable in homogeneous samples; (2) the high-frequency signals are distorted by and do not readily penetrate conductive materials, due to the skin effect; and (3) high-field magnets are somewhat bulky, expensive, and are generally designed for studying samples in NMR tubes, and they cannot be deployed easily for certain in-field applications, such as point-of-care diagnostics.

These disadvantages can be circumvented through the use of an alternative modality, zero- to ultralow-field (ZULF) NMR, in which measurements are performed in the absence of a strong magnetic field.[7,8] In this field regime, chemical shifts are negligible, and the dominant nuclear-spin interactions are spin−spin (J) couplings, which are typically on the order of Hz to hundreds of Hz. At these low frequencies, conductive materials have a negligible effect on signals, and because susceptibility-induced magnetic-field gradients are proportional to the applied field strength, resolution is unaffected even in complex heterogeneous samples.[9,10] Even though ZULF spectra do not contain chemical-shift information, individual molecules can still be identified with high specificity, since the J-couplings provide a means of chemical fingerprinting.[11−13] This is especially simple for hyperpolarized systems in which only selected chemical species are initially hyperpolarized and only these molecules and their downstream products contribute to the observable signal.

Received: May 13, 2023
Accepted: September 11, 2023
Published: December 4, 2023

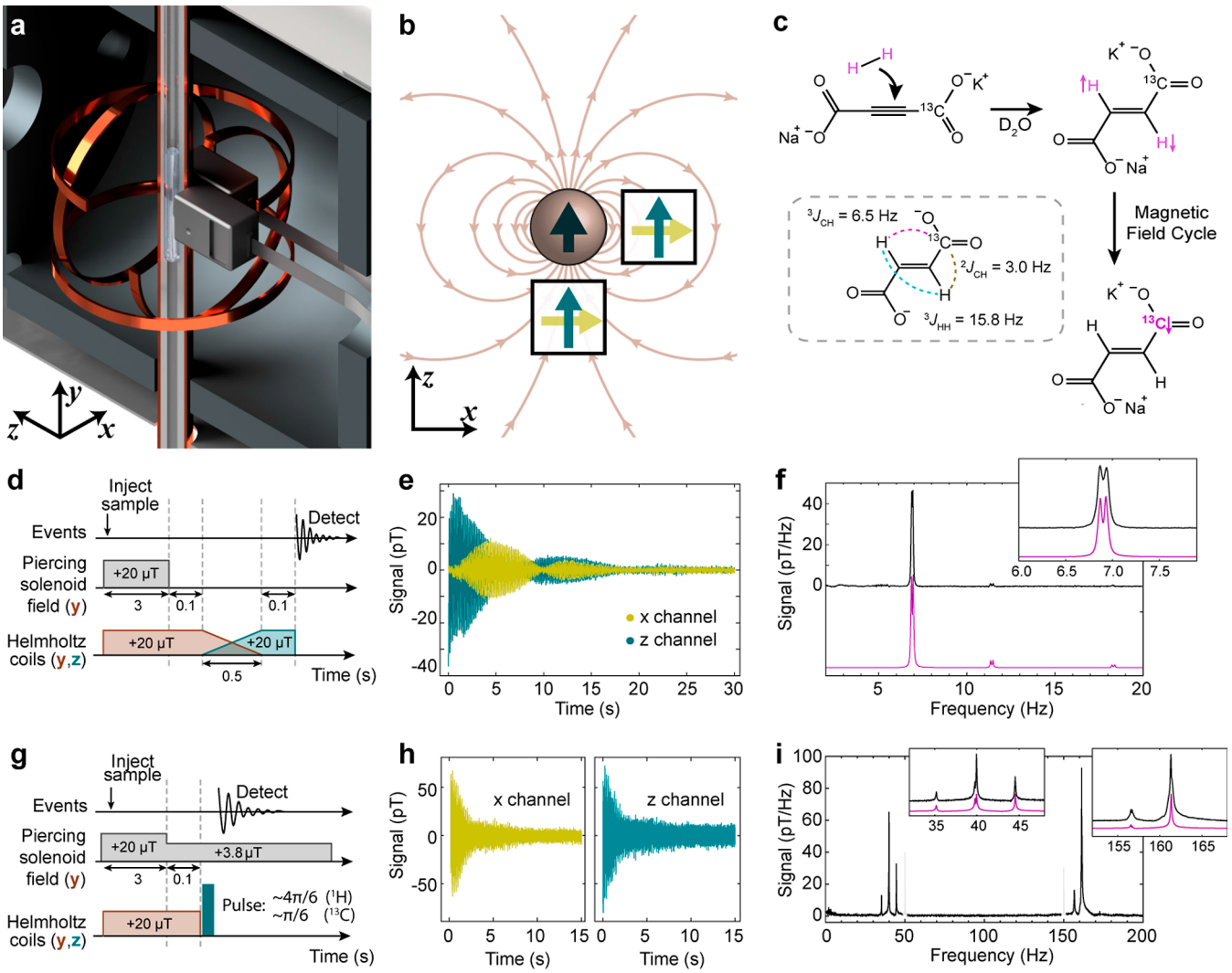

Figure 1. Measurement of hyperpolarized [1-^{13}C]fumarate. (a) Experimental apparatus, with cutaways from the shield and coils for clarity. (b) Schematic of the QZFM OPM placement around the sample, showing the sensitive axes of the OPMs and the magnetic field lines of a magnetic sample polarized along the *z* axis. (c) The hyperpolarization process for [1-^{13}C]fumarate. The [1-^{13}C]fumarate *J*-couplings are shown in the inset. (d) Magnetic field "pulse" sequence used for the zero-field experiments. (e) Zero-field time-domain signal measured along the *x*- and *z*-axes of the OPMs generated from a sample of ^{13}C polarized [1-^{13}C]fumarate. (f) Zero-field spectrum (black) resulting from the Fourier transform of the *z*-axis signal. A simulated spectrum is shown beneath in magenta. (g) Magnetic field "pulse" sequence used for the low-field experiments. (h) Low-field time-domain signal measured along the *x*- and *z*-axes of the OPMS generated from a sample of ^{13}C polarized [1-^{13}C]fumarate. (i) Low-field spectrum (black) resulting from the Fourier transform of the *z*-axis signal. A simulated spectrum is shown beneath in magenta.

Nevertheless, at such low frequencies of the electromagnetic signals, inductive detection is inefficient, and ZULF NMR has relied on highly sensitive superconducting quantum interference devices (SQUIDs), and more recently on optically pumped magnetometers (OPMs), that are able to detect magnetic signals with sensitivities on the order of $fT/\sqrt{Hz}$.[14,15] The primary use of OPMs is for magnetoencephalography (MEG), which is a separate technique for mapping out brain activity based on the magnetic fields produced by neuronal currents.[16,17] Despite the exquisite sensitivity offered by the OPMs, detection of zero-field NMR signals is approximately 2 to 3 orders of magnitude less sensitive than inductive detection at ca. 7 T, assuming the same spin polarization and the same sample/detector geometry. The lower sensitivity of ZULF NMR has so far generally precluded applications, especially in a biomedical context, given the intrinsically low concentrations of metabolites in biological systems.

In this work, we combine recent advances in parahydrogen-based hyperpolarization methods with state-of-the-art magnetometry to demonstrate that enzymatic transformations can be observed using a portable zero- and low-field NMR spectrometer. We study two model processes: the conversion of fumarate into malate, which is used in vivo as a marker of cell necrosis,[18] and the conversion of pyruvate into lactate, which is by far the most widely studied metabolic process in hyperpolarization-enhanced imaging.[19] Hyperpolarized ^{13}C-labeled metabolites were prepared via parahydrogen-induced polarization (PHIP),[20,21] which involves chemically reacting a precursor molecule with molecular hydrogen in the nuclear-spin singlet state (parahydrogen) to yield a hyperpolarized product molecule. The entangled state of the ^{1}H nuclear-spin pair can be converted into a magnetic state of the ^{13}C spin via a magnetic field sweep.[22,23] Preparing the molecules in a ^{13}C-

https://doi.org/10.1021/acs.analchem.3c02087
Anal. Chem. 2023, 95, 17997−18005

polarized state facilitates detection, since as long as a magnetic field of $\gtrsim$1 μT is applied to the sample, the ^{13}C nuclei will remain polarized during chemical transformations. We compare zero- and low-field NMR for these experiments and in the context of reaction monitoring and discuss the advantages and disadvantages of the two approaches.

2. MATERIALS AND METHODS

2.1. Zero and Low-Field NMR Spectrometer. A simplified rendering of the zero- and low-field NMR spectrometer is shown in Figure 1a. To achieve close to zero magnetic field (<2 nT) inside the spectrometer, it was built a four-layer magnetic shield, with built-in B_x, B_y, and B_z shim coils (Twinleaf LLC). A set of three orthogonal Helmholtz coils were present inside the shield to generate pulsed magnetic fields for control of the spin states and their dynamics. Finally, a long solenoid coil pierced through the magnetic shield (a "piercing solenoid") along the y axis, to allow for a magnetic field to be applied locally at the position of the sample but not the detectors.[24] The ratio of the internal and stray fields at the sample and detector, respectively, was 500.

The sample to be measured was loaded in a 5 mm glass NMR tube, which was passed through the piercing solenoid into the magnetic shield, and measured with two QuSpin QZFM Gen-2 OPMs.[25] Each QZFM was sensitive to the x-axis ($B_x(t)$) and z-axis ($B_z(t)$) magnetic fields produced by the sample. The standoff distance from the center of the QZFM atomic vapor cell to the outside of the housing was 6.5 mm, and the piercing solenoid had a radius of 7 mm, giving a sensor-to-sample standoff distance of 13.5 mm. The staggered arrangement of the magnetometers was chosen to reduce common-mode noise while maximizing the signal from the sample, a gradiometric detection scheme.[26] As illustrated in Figure 1b, the magnetic field produced by the nuclear spins in the sample has opposite signs at the locations of the two sensors. In contrast, many noise sources that are centered further from the detectors (e.g., Johnson noise from the magnetic shielding or magnetic fluctuations in the room) produce magnetic fields that are more homogeneous at the positions of the OPMs. By measuring the difference in the outputs from the two sensors, signals from the sample are combined constructively, and common-mode noise is canceled. Because the sensors have two sensitive axes, it was possible to independently measure magnetic fields corresponding to magnetization along x and z.

2.2. Hyperpolarization of Fumarate and Pyruvate. Parahydrogen at >95% enrichment was generated by passing hydrogen gas (>99.999% purity) over a hydrated iron oxide catalyst in a cryostat operating at 30 K. All chemicals used in this work were purchased from Sigma-Aldrich.

To generate solutions of hyperpolarized [1-^{13}C]fumarate, we bubbled parahydrogen gas through a precursor solution (250 mM sodium potassium acetylene dicarboxylate, 250 mM sodium sulfite, and 7 mM $[RuCp^*(CH_3CN)_3]PF_6$ in D_2O) at 8.5 bar and 85 °C for 60 s. A magnetic field cycle was applied to transform the parahydrogen-derived proton singlet order into ^{13}C magnetization.[27] Using this method, we produced solutions of approximately 80 mM [1-^{13}C]fumarate at ~30% ^{13}C polarization. Unless otherwise stated, experiments were performed at a natural ^{13}C abundance. The reaction scheme is shown in Figure 1c, and further details are provided in the Supporting Information.

To generate solutions of hyperpolarized [1-^{13}C]pyruvate, we used the side arm hydrogenation method.[28] We prepared a precursor solution of 400 mM propargyl pyruvate and 20 mM $[Rh(dppb)(COD)]BF_4$ in a solvent of 95:5 (v/v) $CDCl_3$/ethanol-d_6 by dissolving the catalyst in the solvent and adding the propargyl pyruvate immediately (tens of seconds) before each experiment. The sample was heated to 120 °C and hydrogenated for 4 s with parahydrogen at 7 bar. A magnetic field cycle was applied to convert the proton singlet order to ^{13}C polarization. After this, the [1-^{13}C]pyruvate was mixed with 300 μL 400 mM NaOH at 80 °C to cleave the allyl side arm. The aqueous phase containing pyruvate was extracted into a phosphate buffer solution to yield a solution of approximately 80 mM [1-^{13}C]pyruvate at ~ 3.5% ^{13}C polarization. All experiments were performed with [1-^{13}C]-pyruvate (100% ^{13}C-enriched). Further details are given in the Supporting Information.

2.3. Zero- and Low-Field NMR Experiments. For the zero- and low-field NMR experiments to observe [1-^{13}C]-fumarate or [1-^{13}C]pyruvate, the molecules were hyperpolarized as described above and then injected into a 5 mm NMR tube. This was placed in the zero-field spectrometer for signal acquisition.

For the experiments to observe fumarate to malate conversion, 150 μL of the hyperpolarized fumarate sample was injected into a 5 mm NMR tube containing the enzyme fumarase in 450 μL 500 mM phosphate buffer solution at pH 7. The NMR tube was shaken for 5 s and then placed in the zero-field spectrometer for signal acquisition 5 s later, allowing a total of 10 s for the reaction.

For the experiments to observe pyruvate to lactate conversion, the syringe used to extract the aqueous phase from the 10 mm NMR tube contained 200 μL of acidified phosphate buffer solution such that, after mixing, the solution ended at pH 7. Another 100 μL of phosphate buffer solution contained 50 mg NADH and 25 μL of lactate dehydrogenase, and this solution was held in the 5 mm NMR tube. The pyruvate solution was injected into the 5 mm NMR tube and mixed with the enzyme solution by vigorous shaking for 5 s, before being placed into the zero-field spectrometer for signal acquisition 5 s later, allowing a total of 10 s for the reaction.

A modified experimental procedure from the established protocol reported in ref 29 was adopted to increase the volume of the solution and maximize pyruvate concentration (and hence signal) for this proof-of-concept demonstration.

2.4. Data Processing. All signal processing for zero- and low-field experiments was performed using Wolfram Mathematica.[30] The reported x- and z-axis signals were taken as the difference in the measured $B_x(t)$ and $B_z(t)$ fields from the two QZFM sensors. Slow background drifts in the magnetic-field signal were removed by subtracting the moving average from the raw data. Then the first 20−30 ms of data was removed and reconstructed via backward prediction to reduce first-order phase distortions. The z and x measurements were then combined together to yield a complex signal [i.e., $B_z(t) + iB_x(t)$], which was then apodized by multiplying by a decaying exponential. The time-domain signal was then Fourier transformed, followed by a baseline correction. Zero-order phase correction was applied when necessary to produce in-phase spectra.

https://doi.org/10.1021/acs.analchem.3c02087
Anal. Chem. 2023, 95, 17997−18005

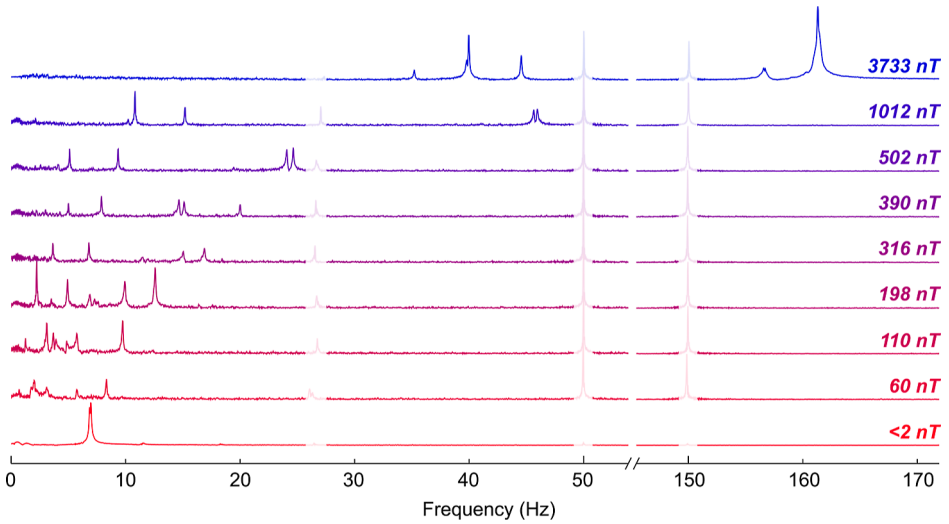

Figure 2. Zero- to low-field NMR spectra of [1-^{13}C]fumarate, measured using the pulse sequence in Figure 1g (or Figure 1d for the <2 nT spectrum) at different background magnetic fields. Noise peaks at 27, 50, and 150 Hz corresponding to line noise and electronic noise from the sensor[25] have been partially grayed-out for clarity.

3. RESULTS

3.1. Zero- and Low-Field NMR Experiments with [1-^{13}C]fumarate. Initial experiments to develop and test the pulse sequences for zero- and low-field experiments were carried out using the hyperpolarized contrast agent [1-^{13}C]-fumarate, since Solutions of hyperpolarized [1-^{13}C]fumarate were produced at ∼80 mM concentration and ∼30% ^{13}C polarization, and the zero field NMR spectrometer are given in the Materials and Methods.

In this work, NMR experiments were performed in two field regimes: zero field, defined as the regime where the nuclear Larmor frequencies are negligible compared to the electron-mediated indirect spin−spin (J) coupling, and low field, where the nuclear Larmor frequencies are larger than the J-couplings but chemical shifts are smaller than the resonance width. The pulse sequence for the zero-field NMR experiments is shown in Figure 1d. The magnetization is rotated from the y axis to the z axis, after which the applied magnetic fields are suddenly turned off, resulting in the magnetic signal shown in Figure 1e. The spectrum resulting from the Fourier transform of this signal is shown in Figure 1f. The main feature is the peak at 6.9 Hz with additional minor peaks at 11.5 and 18.2 Hz, all split by ∼100 mHz due to a 2 nT residual orthogonal field that was not fully shimmed out. The relative simplicity of this J-spectrum is because this molecule comprises a simple three-spin system with the magnetic equivalence of the two parahydrogen protons lifted by asymmetric J-couplings to the ^{13}C spin.[31] A simulated spectrum is shown beneath in magenta. All simulations were performed using the SpinDynamica package for Mathematica.[32]

Low-field NMR experiments can be performed by leaving the piercing solenoid on during signal acquisition. As depicted in Figure 1g, the magnetization is kept along the y axis by a 20 μT field for sample injection, after which the field is reduced to a 3.8 μT detection field and the magnetization is rotated to the x-axis by a DC pulse along z, which results in the precessing magnetic signal shown in Figure 1h. The spectrum resulting from the Fourier transform of this signal is shown in Figure 1i. There are two groups of peaks centered at 40 and 160 Hz, corresponding to signals from the ^{13}C and ^{1}H nuclei of [1-^{13}C]fumarate, respectively. Simulated spectra are shown in magenta. The difference in the noise between the magnetic signals in Figure 1e,h is predominantly from the 50 Hz line noise, which is not present in Figure 1e because a low-pass filter was applied to the data during processing.

3.2. Spectra of [1-^{13}C]fumarate in the Intermediate Field Regime. In Figure 2, we show spectra of [1-^{13}C]-fumarate measured under different background fields, spanning the range between the zero- and low-field regimes. The spectra were acquired using the pulse sequence shown in Figure 1g with the exception of the <2 nT spectrum that was measured using the pulse sequence in Figure 1d. The magnetic field pulse was set to induce a $4\pi/6$ rotation of protons and $\pi/6$ rotation of ^{13}C nuclei so that both nuclei were excited. The spectra exhibit increasing complexity as the field increases and the Zeeman interaction term, which is of the form $B|\gamma_H - \gamma_C|$, approaches the magnitude of the J-couplings.[33] The number of spectral lines decreases again as the term $B|\gamma_H - \gamma_C|$ begins to dominate and the spectral lines group into frequency bands corresponding to nuclear spin species. It is for this reason that in this work we carried out experiments in the two distinct field regimes, and not the intermediate field regime.

3.3. Enzyme-Catalyzed Conversion of Fumarate to Malate. A reaction solution was prepared with 50% ^{13}C labeling in the carboxylate position of the acetylene dicarboxylate. The same chemical reaction with parahydrogen was used to produce [1-^{13}C]fumarate, and following the field cycle to polarize the ^{13}C spin, the solution was mixed with phosphate buffer solution containing a varied amount of fumarase to catalyze the reaction shown in Figure 3a. The reaction was left to proceed for 10 s at Earth's field, after which the solution was measured at zero field using the procedure shown in Figure 1d. The experiment was repeated three times with differing amounts (0, 21, and 52 U, where U is enzyme units) of the enzyme, fumarase, to demonstrate how the resulting spectra change as a function of enzymatic activity. This level of fumarase activity is consistent with reported plasma concentrations following acute kidney injury.[34] Further experimental details are provided in Materials and Methods.

The resulting zero-field NMR spectra are shown in Figure 3b, and feature peaks at 6.9, 11.5, and 18.2 Hz corresponding

https://doi.org/10.1021/acs.analchem.3c02087
Anal. Chem. 2023, 95, 17997−18005

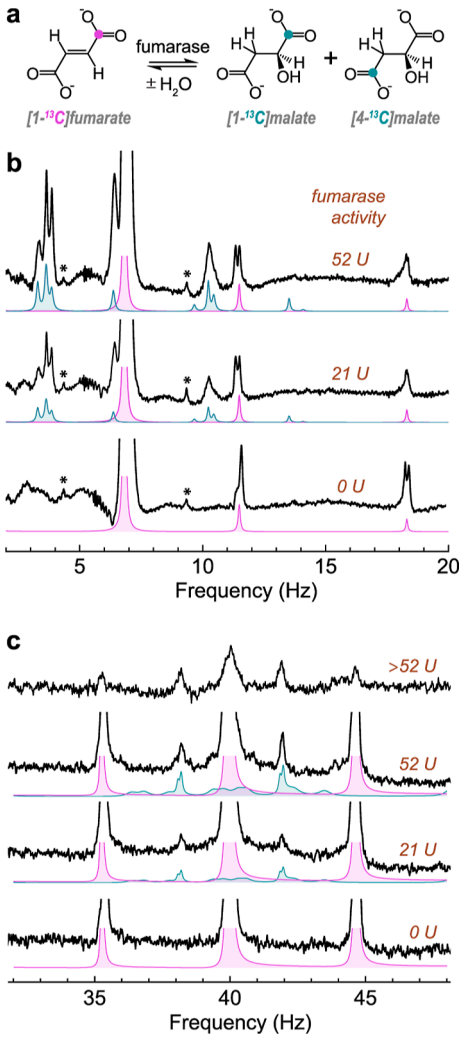

Figure 3. (a) The enzyme-catalyzed interconversion between fumarate and malate. The addition of H_2O breaks the molecular symmetry, and the 1-^{13}C spin label in fumarate has an equal chance to end up in either the 1- or 4- position in malate. (b) Zero-field NMR spectra of the reaction solution. The peaks highlighted with asterisks are carbon satellites from the nuclei of [1,4-$^{13}C_2$]fumarate molecules. (c) Low-field NMR spectra at 3.8 μT of the reaction solution. The amount of fumarase enzyme added to each hyperpolarized fumarate solution prior to detection is shown in brown. All spectra are shown with 50 mHz line broadening. Simulations are shown beneath the spectra in pink and teal for fumarate and malate, respectively. The simulated spectra are vertically scaled to match the real spectra (see Supporting Information for further details about the simulated spectra, including all spin coupling parameters used).

to [1-^{13}C]fumarate and peaks at 3.3, 3.6, 3.9, 6.5, and 10.2 Hz corresponding to [1-^{13}C] and [4-^{13}C]malate. The malate peaks are visible for molecules that formed prior to zero-field detection. The enzymatic reaction does not reach equilibrium on the short time scale of this experiment, and so the malate peaks are largest when 52 U of enzyme was used, since more malate formed prior to detection. Simulated spectra for fumarate and malate are shown in pink and teal, respectively, and are generally in agreement with the experimental data (details of the simulations are provided in the Supporting Information). The signals are well resolved, even for partially overlapping signals at 6.5 and 6.9 Hz. The peak broadening and splittings seen in Figure 3b for e.g., the fumarate peaks at 11.5 and 18.2 Hz are caused by small residual fields on the order of 1 nT orthogonal or parallel to the detection axis, which induce a different splitting of each peak.

Low-field NMR experiments were also performed following the same protocol as above, but using the detection procedure shown in Figure 1g. The resulting ^{13}C spectra are shown in Figure 3c. The fumarate yields a characteristic 1:2:1 triplet peak pattern centered at 40 Hz, and malate peaks appear at approximately 38 and 42 Hz. There are additional malate peaks visible in the simulations but not the spectra, but these are of significantly lower amplitude. If relaxation effects are neglected, then the peaks are all of similar amplitude. To get a better match to the experimental results, dipole−dipole relaxation between the geminal proton pair in malate was included in the simulations. The dipole−dipole relaxation assumed a dipolar coupling of 25 kHz between the protons and a rotational correlation time of 50 ps. This relaxation mechanism was introduced for a 10 s period prior to the pulse and during signal acquisition. Importantly, this relaxation mechanism has a negligible effect on the peaks at 38 and 42 Hz, but the amplitude is much lower than that of the malate peaks in the zero-field spectra. We hypothesize that there is an additional relaxation mechanism related to hydroxyl proton exchange that is effective at low fields (see Discussion).

3.4. Enzyme-Catalyzed Conversion of Pyruvate to Lactate. The metabolic conversion of pyruvate to lactate (Figure 4a) is by far the most-studied in hyperpolarization-enhanced MRI experiments,[4,5] with over 25 clinical trials currently recruiting or underway around the world.[35] To study zero- and low-field spectra of [1-^{13}C]pyruvate and [1-^{13}C]-lactate, we produced hyperpolarized pyruvate using the method described in Materials and Methods. This solution was either observed directly or mixed with a solution containing lactate dehydrogenase and NADH (nicotinamide adenine dinucleotide) and allowed to react for 10 s at Earth's field, after which the solution was measured. The concentration of NADH in the solutions was 150 mM, an excess compared to the 80 mM pyruvate, so complete conversion to lactate would be expected if the reaction was given sufficient time to go to completion.

The zero-field results obtained by applying the pulse sequence from Figure 1d are shown in Figure 4b. The bottom spectrum shows hyperpolarized [1-^{13}C]pyruvate, which is an XA_3 spin system (one ^{13}C and three methyl protons), which exhibits peaks at J_{AX} and $2J_{AX}$, where J_{AX} is approximately 1.4 Hz. Above is the spectrum for the sample to which lactate dehydrogenase and an excess of NADH were added, and this shows a number of additional peaks at frequencies up to 18 Hz. Simulations of the pyruvate and lactate zero-field spectra are shown beneath pink and teal, respectively.

The low-field results obtained by applying the pulse sequence from Figure 1g are shown in Figure 4c. The pyruvate spectrum exhibits the same pattern as would be observed at high-field: the ^{13}C lines are centered at 41 Hz due to the 3.83 μT background magnetic field, and a 1:3:3:1 quartet is observed due to the ^{13}C coupling to the three protons. A central peak can be observed at 41 Hz, which corresponds to a small [1-^{13}C]parapyruvate impurity, which we confirmed by repeating the experiment and seeing a [1-^{13}C]parapyruvate peak without observable J-couplings in a high-field ^{13}C NMR spectrum.[36] The production of lactate can also be seen at low field; a multiplet corresponding to lactate can be resolved in addition to the pyruvate quartet (Figure 4c). Simulations of

https://doi.org/10.1021/acs.analchem.3c02087
Anal. Chem. 2023, 95, 17997−18005

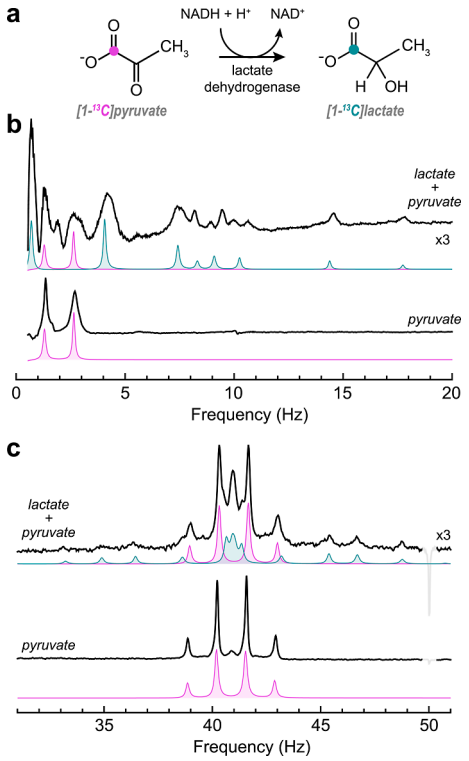

Figure 4. (a) The enzyme-catalyzed conversion of pyruvate to lactate. (b) Zero-field NMR spectra of the reaction solution. (c) Low-field NMR spectra of the reaction solution. For the pyruvate spectra the signal of hyperpolarized pyruvate was acquired directly. For the spectra that show lactate signals, lactate dehydrogenase and an excess of NADH was added to the hyperpolarized pyruvate solution prior to detection. All spectra are shown with 250 mHz line broadening. The 10 Hz peak is a noise artifact, also observable with no sample present. Simulations are shown beneath the spectra in pink and teal for pyruvate and lactate, respectively. The simulated spectra are vertically scaled to match the real spectra (see Supporting Information for further details about the simulated spectra, including all spin coupling parameters used).

the pyruvate and lactate low-field spectra are shown in pink and teal, respectively.

3.5. Experiments on a Microfluidic Platform. Microfluidic lab-on-a-chip platforms are commonly used for biology, so to take a first step in this direction, we carried out an experiment to observe [1-^{13}C]fumarate in a lab-on-a-chip device, rather than in a 5 mm NMR tube. The ZULF apparatus was modified to accommodate a polycarbonate microfluidic chip inside the magnetic shield, with an OPM directly under the 10 μL sample chamber and a pulse coil to apply magnetic fields to the sample to excite NMR signals. We carried out the hyperpolarization procedure described above to produce [1-^{13}C]fumarate (at natural isotopic ^{13}C abundance) and injected the hyperpolarized solution through a solenoid guiding field into the shield and into the microfluidic chip. The pulse coil was holding a constant 16 μT magnetic field, and after 5 s, this field was switched off and the resulting zero-field NMR signal was detected. A schematic of the apparatus is shown in Figure 5a, and the NMR spectrum obtained from this experiment is shown in Figure 5b. Further experimental details are provided in the Supporting Information.

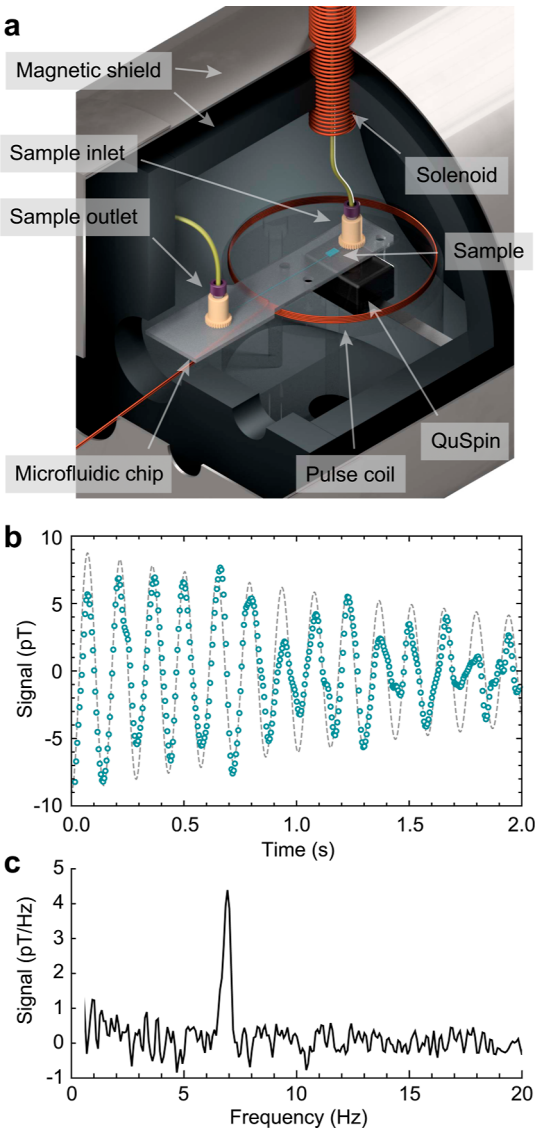

Figure 5. Measurement of hyperpolarized [1-^{13}C]fumarate (without ^{13}C-enrichment) in a microfluidic chip. (a) The experimental setup, showing the microfluidic chip resting on top of a 3D-printed former (made transparent for clarity), which supports a coil and houses the OPM directly beneath the 10 μL sample chamber. The PTFE fluid inlet and outlet lines are shown in yellow, and the inlet passes through a guiding solenoid into the shield. (b) The first 2 s of the NMR signal obtained from a sample of [1-^{13}C]fumarate in the chip (shown by teal circles). A background time signal was acquired by repeating the experiment without a hyperpolarized sample and we show the difference between the real and background signals. A 10 Hz low-pass filter was applied to remove 50 Hz line noise, and one in five acquired data points is shown for clarity. A decaying sinusoidal function of the form $S(t) = -9 \cos(2\pi\, 6.95\, t)\, e^{-t/2.5}$ is overlaid on the data in gray. (c) The Fourier transform of the NMR signal without the low-pass filter applied, with 150 mHz line broadening.

4. DISCUSSION

We have shown that zero- and low-field NMR can be used to measure key steps of metabolic pathways using hyperpolarized molecules. We chose these two reactions to validate our method since they have been studied extensively using high-field NMR and in imaging experiments at high field.[5,6] In work bridging the gap from high-field to low-field, Korchak et al. observed conversion of PHIP-polarized pyruvate into lactate at

https://doi.org/10.1021/acs.analchem.3c02087
Anal. Chem. 2023, 95, 17997−18005

24 mT: they observed the 2-^{13}C isotopomers and used a more-conventional NMR coil for inductive detection to pick up the ∼250 kHz NMR signals.[37] We consider this to be at the boundary between high- and low-field NMR, since the spectra have chemical shift resolution, but at 22 mT they leverage many of the advantages of low-field NMR (e.g., lack of heterogeneous line broadening and setup portability). However, at 250 kHz rf frequency the skin depth of, e.g., stainless steel is 870 μm, whereas for the ∼40 Hz low-field signals in our experiments, the skin depth is ∼6.9 cm. We believe that this lower-field approach with OPM-based detection is necessary for detecting samples in/near metals.

We observe that the signals from the converted metabolites malate and lactate are lower at elevated (3.8 μT) fields compared to zero field, which is not the case for fumarate and pyruvate. We attribute this to faster relaxation of malate and lactate at microtesla fields, which may be related to the fact that the rate of hydroxyl exchange is approximately 350 s^{-1} at pH 7 and 25 °C.[38] This is close to nuclear spin Larmor frequencies at microtesla field strengths, so the fluctuating dipolar field from exchanging protons may act as a relaxation mechanism. We performed additional experiments in which we formed [1-^{13}C]lactate directly via side arm hydrogenation and allowed it to relax for a fixed time at variable field, followed by measurement of the ^{13}C polarization. From these experiments, we determined that above a field of ∼30 μT, the proposed hydroxyl exchange relaxation mechanism is no longer dominant. These results are presented in the Supporting Information.

In the zero-field experiments, the magnetic field sequence to generate the signals was chosen such that the reaction solution remained at relatively high field until signal detection. The reason for this is that the hyperpolarization remains as Zeeman order on the ^{13}C nucleus during the chemical reaction, so the change in J-coupling topology does not significantly affect the hyperpolarized spin order. We expect that if the reactions occurred at zero field, the change in the J-coupling Hamiltonian, which occurs at different time points for each molecule, would cause loss of coherence and, hence, significant polarization losses.[39] It is only immediately before signal acquisition that the magnetic field is switched to zero, and we observe malate/lactate that formed prior to this; i.e., we do not see the molecules that form during signal acquisition.

Generally, high-field magnetic resonance imaging of metabolism using hyperpolarized biomolecules is performed using a train of small-angle pulses so as not to significantly perturb the hyperpolarized spin order in each experiment. This allows one to collect a time-series of spectra to study metabolic flux and extract information about the reaction kinetics. By contrast, in the experiments reported here, the magnetic field sequence converts the hyperpolarized spin order into observable signals that are detected once; in this sense, it is a "single-shot" experiment. We carried out additional experiments in a separate ZULF device with a single QZFM, observing [1-^{13}C]pyruvate with 15° pulses applied every 6.5 or 8.2 s. The [1-^{13}C]pyruvate was polarized via dynamic nuclear polarization (12−13% polarization) and injected into a suspension of 5 million HeLa cells in a 10 mm NMR tube. We observed the [1-^{13}C]pyruvate signal decay over time, but we were unable to observe [1-^{13}C]lactate in these experiments, due to the lower signal-to-noise ratio of this apparatus and when using cells rather than a pure enzyme. See Supporting Information for further details and spectra. Under similar experimental conditions but with detection carried out in a 1.4 T benchtop magnet, we are able to observe [1-^{13}C]lactate formation in time-resolved experiments. This result highlights that this technology, while promising as an alternative to high-field NMR, suffers from lower sensitivity and is not yet at the point of in vivo application.

Quadrupolar nuclei at zero field can act as relaxation sink. At zero field, nuclear spins with mutual J-coupling become strongly coupled, since the Zeeman energy differences are absent and the J-coupling between them dominates. Consider two spins with a difference in Zeeman polarization that become strongly coupled in a nonadiabatic manner (e.g., by quickly turning off an external magnetic field or by chemical reaction); the polarization of the two spins will begin to exchange in an oscillatory manner, with the frequency given by the J-coupling. This oscillating magnetization is the observable in many zero-field NMR experiments. However, this makes the hyperpolarized spin order particularly sensitive to the presence of J-coupled quadrupolar nuclei (e.g., ^{2}H or ^{14}N), since polarization that oscillates onto these spins can rapidly relax.[40] This is not a problem in the low-field experiments. In fumarate experiments, the reaction to generate fumarate is carried out in D_2O to prolong the hyperpolarization lifetime, but the conversion to malate should not be carried out in pure D_2O since all malate molecules would then contain deuterium. We performed separate experiments in which the enzyme reaction was carried out in pure D_2O, and observed fumarate signals but no NMR signals from malate. For this reason, we used a 1:1 H_2O/D_2O mixture as the solvent for the metabolic reaction, so approximately 50% of the malate molecules are protonated rather than deuterated. Novel methods now enable decoupling of deuterium nuclei, which should help to alleviate this problem by suppressing the polarization exchange.[41,42] Regardless, for in vivo experiments, the fumarate would first be purified and then brought into an H_2O solution using established methods.[43]

The gradiometric detection scheme used in this work is shown schematically in Figure 1b. Taking the sample to be a long cylinder homogeneously magnetized transverse to the cylindrical axis, the resulting magnetic field takes a two-dimensional dipole shape such that the field magnitude is constant at a given radius from the center of the sample. Hence, in these experiments, the signal was acquired simultaneously in both the x- and z-channels of two QZFM OPMs, and during processing the signal, difference was taken for each axis. This gradiometric detection scheme has two advantages: (1) the observable signal is enhanced by detecting with multiple sensors (up to a factor of 2) and (2) acquiring the differential signal is an effective way to cancel common-mode noise (magnetic noise that is the same at the positions of both OPMs).

In this work the low-field experiments were carried out at relatively low frequency (<200 Hz) since the bandwidth of the magnetometers here was 135 Hz. This is certainly not a fundamental limitation of the commercial OPMs used in this work, which have been shown to be capable of operation at up to 1.7 kHz.[44]

Most experiments were carried out with 5 mm NMR tubes, with a sample volume of ∼600 μL, and a detected volume of approximately 100−200 μL. In the microfluidic experiment, we were able to observe a 10 μL sample in a single scan, albeit with a reduced signal-to-noise ratio. A quantitative comparison between the signal in macro- and microfluidic experiments is

https://doi.org/10.1021/acs.analchem.3c02087
Anal. Chem. 2023, 95, 17997−18005

challenging due to the different experimental procedures that were employed to obtain the spectra. Although the microfluidic chip used did not involve fluidic complexity, this is a strength of lab-on-a-chip devices, and indeed it has been shown that the chemical reaction to hyperpolarize fumarate can be carried out on a chip.[45] Microfluidic NMR is hindered in widespread use in part due to the need for specially designed probes for high-field implementation as well as limited resolution due to magnetic field gradients at the interface between the chip and sample; ZULF NMR does not suffer from these limitations and might prove to be a useful spectroscopic technique in this field.

5. CONCLUSIONS

In this work, we have used a gradiometer based on OPMs to observe the conversion of [1-^{13}C]fumarate to [1-^{13}C]malate and [4-^{13}C]malate, and [1-^{13}C]pyruvate to [1-^{13}C]lactate at both zero- and low-field. We also report zero-field NMR spectroscopy of hyperpolarized [1-^{13}C]fumarate at natural ^{13}C abundance in a microfluidic chip. Since high-field NMR requires specially designed probes to accommodate lab-on-a-chip devices, low-field NMR may provide a compelling alternative, although it is likely that the sensitivity would need to be improved for widespread applications in this direction.

For many applications, we consider the low-field experiment to be preferable to the zero-field experiment in a few ways: (1) Zeeman order is not strongly perturbed by chemical transformations since the spin topology changes are small; (2) quadrupolar nuclei do not act as relaxation sinks; (3) poor shimming of the magnetic field does not broaden/split the lines so severely; and (4) the signal frequencies can be chosen by varying the field, to avoid coincidence with noisy spectral regions. However, the low-field experiment requires a slightly more complex experimental setup with a piercing solenoid or other means of producing a field at the position of the sample but not the detector.

We believe this work represents an exciting technological development, but note that the step to in vivo applications will require further sensitivity improvements due to the greater distance between the sensor and sample and the lower concentration of biomolecules in vivo. In the Supporting Information, we discuss further the possibility for in vivo experiments and provide an estimate of expected detection sensitivity. A particular appeal of OPM detection is that the advanced magnetometer arrays and image reconstruction algorithms that have been made available for MEG[17] could be used directly for low-field metabolic MRI. There is also the exciting future possibility of a combined MEG/MRI modality capable of simultaneously measuring electromagnetic neuronal activity, brain metabolism, and correlations between the two.

■ ASSOCIATED CONTENT

Supporting Information

The Supporting Information is available free of charge at https://pubs.acs.org/doi/10.1021/acs.analchem.3c02087.

Additional details about experimental methods and how simulations were performed, additional experiments with DNP-polarized [1-^{13}C]pyruvate at low field, sensitivity estimation for low-field in vivo imaging, and additional relaxation experiments carried out on PHIP-polarized [1-^{13}C]pyruvate and [1-^{13}C]lactate (PDF)

■ AUTHOR INFORMATION

Corresponding Author

James Eills − *Barcelona Institute of Science and Technology, Institute for Bioengineering of Catalonia, Barcelona 08028, Spain; GSI Helmholtzzentrum für Schwerionenforschung, Helmholtz-Institut Mainz, Mainz 55128, Germany; Institute for Physics, Johannes Gutenberg-Universität Mainz, Mainz 55099, Germany;* orcid.org/0000-0001-8468-6860; Email: jeills@ibecbarcelona.eu

Authors

Román Picazo-Frutos − *GSI Helmholtzzentrum für Schwerionenforschung, Helmholtz-Institut Mainz, Mainz 55128, Germany; Institute for Physics, Johannes Gutenberg-Universität Mainz, Mainz 55099, Germany;* orcid.org/0000-0002-6190-1975

Oksana Bondar − *Department of Molecular Biotechnology and Health Sciences, Center of Molecular Imaging, University of Turin, Turin 10126, Italy;* orcid.org/0000-0003-0686-1509

Eleonora Cavallari − *Department of Molecular Biotechnology and Health Sciences, Center of Molecular Imaging, University of Turin, Turin 10126, Italy*

Carla Carrera − *Institute of Biostructures and Bioimaging, National Research Council of Italy, Turin 10126, Italy;* orcid.org/0000-0002-1571-7851

Sylwia J. Barker − *School of Chemistry, University of Southampton, Southampton SO17 1BJ, U.K.;* orcid.org/0000-0001-7867-5938

Marcel Utz − *School of Chemistry, University of Southampton, Southampton SO17 1BJ, U.K.;* orcid.org/0000-0003-2274-9672

Alba Herrero-Gómez − *Barcelona Institute of Science and Technology, Institute for Bioengineering of Catalonia, Barcelona 08028, Spain;* orcid.org/0000-0002-8807-0649

Irene Marco-Rius − *Barcelona Institute of Science and Technology, Institute for Bioengineering of Catalonia, Barcelona 08028, Spain;* orcid.org/0000-0001-5076-8526

Michael C. D. Tayler − *The Barcelona Institute of Science and Technology, ICFO—Institut de Ciéncies Fotóniques, Barcelona 08860, Spain;* orcid.org/0000-0002-9977-8204

Silvio Aime − *Department of Molecular Biotechnology and Health Sciences, Center of Molecular Imaging, University of Turin, Turin 10126, Italy*

Francesca Reineri − *Department of Molecular Biotechnology and Health Sciences, Center of Molecular Imaging, University of Turin, Turin 10126, Italy*

Dmitry Budker − *GSI Helmholtzzentrum für Schwerionenforschung, Helmholtz-Institut Mainz, Mainz 55128, Germany; Institute for Physics, Johannes Gutenberg-Universität Mainz, Mainz 55099, Germany; Department of Physics, University of California at Berkeley, Berkeley, California 94720, United States;* orcid.org/0000-0002-7356-4814

John W. Blanchard − *GSI Helmholtzzentrum für Schwerionenforschung, Helmholtz-Institut Mainz, Mainz 55128, Germany; Quantum Technology Center, University of Maryland, College Park, Maryland 20742, United States;* orcid.org/0000-0002-1621-6637

Complete contact information is available at:

https://doi.org/10.1021/acs.analchem.3c02087
Anal. Chem. 2023, 95, 17997−18005

https://pubs.acs.org/10.1021/acs.analchem.3c02087

Notes

The authors declare no competing financial interest.

■ ACKNOWLEDGMENTS

This project has received funding from the European Union's Horizon 2020 Research and Innovation Programme under the Marie Skłodowska-Curie Grant Agreement 766402, 101063517, and the FET-Open AlternativesToGd Proposal no. 858149. As well as by the DFG (Project ID 465084791). This work has been supported by an EPSRC iCASE studentship EP/R513325/1 to S.J.B., cofunded by Bruker UK Ltd.

■ REFERENCES

(1) Eills, J.; Budker, D.; Cavagnero, S.; Chekmenev, E. Y.; Elliott, S. J.; Jannin, S.; Lesage, A.; Matysik, J.; Meersmann, T.; Prisner, T.; Reimer, J. A.; Yang, H.; Koptyug, I. V. *Chem. Rev.* **2023**, *123*, 1417−1551. PMID: 36701528

(2) Kuhn, L. T.; Akbey, U. *Hyperpolarization Methods in NMR Spectroscopy*; Springer, 2013; Vol. *338*.

(3) Nikolaou, P.; Goodson, B. M.; Chekmenev, E. Y. *Chem.—Eur. J.* **2015**, *21*, 3156−3166.

(4) Wang, Z. J.; Ohliger, M. A.; Larson, P. E. Z.; Gordon, J. W.; Bok, R. A.; Slater, J.; Villanueva-Meyer, J. E.; Hess, C. P.; Kurhanewicz, J.; Vigneron, D. B. *Radiology* **2019**, *291*, 273−284.

(5) Nelson, S. J.; Kurhanewicz, J.; Vigneron, D. B.; Larson, P. E.; Harzstark, A. L.; Ferrone, M.; Van Criekinge, M.; Chang, J. W.; Bok, R.; Park, I.; et al. *Sci. Transl. Med.* **2013**, *5*, 198ra108.

(6) Gallagher, F. A.; Kettunen, M. I.; Hu, D.-E.; Jensen, P. R.; Zandt, R. i.; Karlsson, M.; Gisselsson, A.; Nelson, S. K.; Witney, T. H.; Bohndiek, S. E.; et al. *Proc. Natl. Acad. Sci. U.S.A.* **2009**, *106*, 19801−19806.

(7) Blanchard, J. W.; Budker, D.; Trabesinger, A. *J. Magn. Reson.* **2021**, *323*, 106886.

(8) Jiang, M.; Bian, J.; Li, Q.; Wu, Z.; Su, H.; Xu, M.; Wang, Y.; Wang, X.; Peng, X. *Fundam. Res.* **2021**, *1*, 68−84.

(9) Tayler, M. C.; Ward-Williams, J.; Gladden, L. F. *J. Magn. Reson.* **2018**, *297*, 1−8.

(10) Burueva, D. B.; Eills, J.; Blanchard, J. W.; Garcon, A.; Picazo Frutos, R.; Kovtunov, K. V.; Koptyug, I. V.; Budker, D. *Angew. Chem., Int. Ed.* **2020**, *59*, 17026−17032.

(11) Blanchard, J. W.; Ledbetter, M. P.; Theis, T.; Butler, M. C.; Budker, D.; Pines, A. *J. Am. Chem. Soc.* **2013**, *135*, 3607−3612.

(12) Alcicek, S.; Put, P.; Kontul, V.; Pustelny, S. *J. Phys. Chem. Lett.* **2021**, *12*, 787−792.

(13) Van Dyke, E. T.; Eills, J.; Picazo-Frutos, R.; Sheberstov, K. F.; Hu, Y.; Budker, D.; Barskiy, D. A. *Sci. Adv.* **2022**, *8*, No. eabp9242.

(14) Li, J.; Quan, W.; Zhou, B.; Wang, Z.; Lu, J.; Hu, Z.; Liu, G.; Fang, J. *IEEE Sens. J.* **2018**, *18*, 8198−8207.

(15) Tayler, M. C. D.; Theis, T.; Sjolander, T. F.; Blanchard, J. W.; Kentner, A.; Pustelny, S.; Pines, A.; Budker, D. *Rev. Sci. Instrum.* **2017**, *88*, 091101.

(16) Boto, E.; Holmes, N.; Leggett, J.; Roberts, G.; Shah, V.; Meyer, S. S.; Muñoz, L. D.; Mullinger, K. J.; Tierney, T. M.; Bestmann, S.; Barnes, G. R.; Bowtell, R.; Brookes, M. J. *Nature* **2018**, *555*, 657−661.

(17) Pratt, E. J.; Ledbetter, M.; Jiménez-Martínez, R.; Shapiro, B.; Solon, A.; Iwata, G. Z.; Garber, S.; Gormley, J.; Decker, D.; Delgadillo, D.; et al. Kernel Flux: a whole-head 432-magnetometer optically-pumped magnetoencephalography (OP-MEG) system for brain activity imaging during natural human experiences. *Optical and Quantum Sensing and Precision Metrology*; SPIE, 2021; p 1170032.

(18) Clatworthy, M. R.; Kettunen, M. I.; Hu, D.-E.; Mathews, R. J.; Witney, T. H.; Kennedy, B. W.; Bohndiek, S. E.; Gallagher, F. A.; Jarvis, L. B.; Smith, K. G.; et al. *Proc. Natl. Acad. Sci. U.S.A.* **2012**, *109*, 13374−13379.

(19) Serrao, E. M.; Brindle, K. M. *Front. Oncol.* **2016**, *6*, 59.

(20) Bowers, C. R.; Weitekamp, D. P. *J. Am. Chem. Soc.* **1987**, *109*, 5541−5542.

(21) Hövener, J.; Pravdivtsev, A. N.; Kidd, B.; Bowers, C. R.; Glöggler, S.; Kovtunov, K. V.; Plaumann, M.; Katz-Brull, R.; Buckenmaier, K.; Jerschow, A.; et al. *Angew. Chem. Int. Ed* **2018**, *57*, 11140−11162.

(22) Golman, K.; Axelsson, O.; Jóhannesson, H.; Månsson, S.; Olofsson, C.; Petersson, J. *Magn. Reson. Med.* **2001**, *46*, 1−5.

(23) Schmidt, A. B.; Bowers, C. R.; Buckenmaier, K.; Chekmenev, E. Y.; de Maissin, H.; Eills, J.; Ellermann, F.; Glöggler, S.; Gordon, J. W.; Knecht, S.; et al. *Anal. Chem.* **2022**, *94*, 479−502.

(24) Yashchuk, V.; Granwehr, J.; Kimball, D.; Rochester, S.; Trabesinger, A.; Urban, J.; Budker, D.; Pines, A. *Phys. Rev. Lett.* **2004**, *93*, 160801.

(25) Blanchard, J. W.; Wu, T.; Eills, J.; Hu, Y.; Budker, D. *J. Magn. Reson.* **2020**, *314*, 106723.

(26) Jiang, M.; Frutos, R. P.; Wu, T.; Blanchard, J. W.; Peng, X.; Budker, D. *Phys. Rev. Applied* **2019**, *11*, 024005.

(27) Eills, J.; Cavallari, E.; Carrera, C.; Budker, D.; Aime, S.; Reineri, F. *J. Am. Chem. Soc.* **2019**, *141*, 20209−20214.

(28) Reineri, F.; Boi, T.; Aime, S. *Nat. Commun.* **2015**, *6*, 5858.

(29) Cavallari, E.; Carrera, C.; Di Matteo, G.; Bondar, O.; Aime, S.; Reineri, F. *Front. Oncol.* **2020**, *10*, 497.

(30) Wolfram, S. *Mathematica: A System for Doing Mathematics by Computer*; Addison-Wesley, 1991.

(31) Eills, J.; Stevanato, G.; Bengs, C.; Glöggler, S.; Elliott, S. J.; Alonso-Valdesueiro, J.; Pileio, G.; Levitt, M. H. *J. Magn. Reson.* **2017**, *274*, 163−172.

(32) Bengs, C.; Levitt, M. H. *Magn. Reson. Chem.* **2018**, *56*, 374−414.

(33) Blanchard, J. W.; Budker, D. *eMagRes.* **2016**, *5*, 1395−1410.

(34) Nielsen, P. M.; Eldirdiri, A.; Bertelsen, L. B.; Jørgensen, H. S.; Ardenkjaer-Larsen, J. H.; Laustsen, C. *Sci. Rep.* **2017**, *7*, 40812.

(35) https://www.clinicaltrials.gov/ (accessed 30/06/23).

(36) Rios, A. C.; Bera, P. P.; Moreno, J. A.; Cooper, G. *ACS omega* **2020**, *5*, 15063−15068.

(37) Korchak, S.; Jagtap, A. P.; Glöggler, S. *Chem. Sci.* **2021**, *12*, 314−319.

(38) DeBrosse, C.; Nanga, R. P. R.; Bagga, P.; Nath, K.; Haris, M.; Marincola, F.; Schnall, M. D.; Hariharan, H.; Reddy, R. *Sci. Rep.* **2016**, *6*, 19517.

(39) Barskiy, D. A.; Tayler, M. C.; Marco-Rius, I.; Kurhanewicz, J.; Vigneron, D. B.; Cikrikci, S.; Aydogdu, A.; Reh, M.; Pravdivtsev, A. N.; Hövener, J. B.; Blanchard, J. W.; Wu, T.; Budker, D.; Pines, A. *Nat. Commun.* **2019**, *10*, 3002.

(40) Barskiy, D.; Blanchard, J. W.; Reh, M.; Sjoelander, T.; Pines, A.; Budker, D. Zero-Field J-spectroscopy of Quadrupolar Nuclei. **2020**, arXiv:2011.05618.

(41) Bodenstedt, S.; Moll, D.; Glöggler, S.; Mitchell, M. W.; Tayler, M. C. *J. Phys. Chem. Lett.* **2022**, *13*, 98−104.

(42) Dagys, L.; Bengs, C.; Moustafa, G. A. I.; Levitt, M. H. *ChemRxiv* **2022**, *23*, No. e202200274.

(43) Knecht, S.; Blanchard, J. W.; Barskiy, D.; Cavallari, E.; Dagys, L.; Van Dyke, E.; Tsukanov, M.; Bliemel, B.; Münnemann, K.; Aime, S.; et al. *Proc. Natl. Acad. Sci. U.S.A.* **2021**, *118*, No. e2025383118.

(44) Savukov, I.; Kim, Y. J.; Shah, V.; Boshier, M. G. *Meas. Sci. Technol.* **2017**, *28*, 035104.

(45) Barker, S. J.; Dagys, L.; Hale, W.; Ripka, B.; Eills, J.; Sharma, M.; Levitt, M. H.; Utz, M. *Anal. Chem.* **2022**, *94*, 3260−3267. PMID: 35147413